Thermal distortions of non-Gaussian beams in Fabry-Perot cavities

J Miller[1,2], P Willems[2], H Yamamoto[2], J Agresti[2,3] and R DeSalvo[2]

[1]IGR, University of Glasgow, University Avenue, Glasgow, G12 8QQ, U.K.
[2]LIGO Laboratory, California Institute of Technology, 1200 E. California Blvd., Pasadena, CA 91125, USA
[3]Dipartimento di Fisica presso Università di Pisa, via Fermi 8, 56126 Pisa, Italy

E-mail: `j.miller@physics.gla.ac.uk`

Abstract. Thermal effects are already important in currently operating interferometric gravitational wave detectors. Planned upgrades of these detectors involve increasing optical power to combat quantum shot noise. We consider the ramifications of this increased power for one particular class of laser beams - wide, flat-topped, mesa beams. In particular we model a single mesa beam Fabry-Perot cavity having thermoelastically deformed mirrors. We calculate the intensity profile of the fundamental cavity eigenmode in the presence of thermal perturbations, and the associated changes in thermal noise. We also outline an idealised method of correcting for such effects. At each stage we contrast our results with those of a comparable Gaussian beam cavity. Although we focus on mesa beams the techniques described are applicable to any azimuthally symmetric system.

1. Introduction

The sensitivity of current kilometre-scale interferometric gravitational wave detectors such as GEO600 [1], Virgo [2], and LIGO [3] is limited by fundamental noise processes. One of these is shot noise in the detected light power and for this reason they operate with kilowatts of stored power. Planned improvements to these detectors will increase this stored power to the hundreds of kilowatts range.

Another fundamental limit to sensitivity is thermal motion of the interferometer mirrors. It is anticipated that the dominating noise source in the middle of the terrestrial gravitational wave detection band will be coating thermal noise [4]. These thermodynamic effects cause the surface of a test mass to fluctuate stochastically on a microscopic scale. Crudely speaking, interferometric gravitational wave detectors operate by measuring the position of their test masses' high reflectivity surfaces weighted by the intensity profile of the arm cavity eigenmode. Narrow, sharply peaked Gaussian beams which meet 1 ppm diffraction loss requirements are not optimal - they provide a poor spatial average of these thermal fluctuations. Heuristically, a wider beam with a more uniform intensity profile will average over a larger number of fluctuations and thus reduce the impact of test mass thermal noise. One such beam which has been proposed for use in gravitational wave interferometers is the mesa beam. This beam has been predicted to reduce mirror thermal noise by around a factor of two relative to a Gaussian beam, without being significantly more difficult to control [5, 6, 7, 8]. The mesa beam resonates in Fabry-Perot cavities with specially tailored aspherical mirror surfaces.

The LIGO detector already employs a thermal compensation system to correct some mirrors' radial profiles against thermal effects arising from absorption of stored optical power [9]. In future high power upgrades, thermal perturbations will be commensurately increased. They will distort the mirror surfaces, changing the structure of the resonant optical mode. In turn this will change the measured thermal noise, and potentially reduce the stored power due to scattering of light out of the fundamental mode of the arm cavities or by degrading the coupling with the injected beam.

We study thermally induced perturbations of a Fabry-Perot cavity in the presence of high circulating power and consider how a thermoelastically distorted test mass affects the intensity profile of the resonant optical mode. We evaluate the thermal noise performance of the new eigenmode and discuss possible methods of compensating for the deformed test masses.

Two cavities supporting non-Gaussian mesa beams are considered, one nearly flat [5, 10], the other nearly concentric [11]. As a foil to these cases we also study a nearly concentric spherical cavity. All three cavities have a length of 4 km. Each mirror of the spherical cavity has a radius of curvature 2076 m and therefore supports well-known Gaussian modes. These parameters are similar to the proposed Advanced LIGO baseline configuration. For each cavity the input beam is that Gaussian beam which is optimally coupled to the unperturbed or 'cold' cavity. This injection beam remains fixed for all calculations in each case.

1.1. Intensity/Mirror profiles

In the unperturbed spherical mirror cavity, the resonant optical field at the mirror surface is a fundamental Gaussian mode. The phase fronts of this beam, and therefore the cavity mirrors, are spherical. For a discussion of Gaussian beams and their properties see, for example, Kogelnik & Li [12].

In the nearly flat cavity case the unnormalised mesa field at the mirror position is given by [10],

$$\Psi_{\text{mesa}}(r) \propto \int_{\vec{r}' \leq D} \exp\left[-\frac{(\vec{r} - \vec{r}')^2(1 - \mathrm{i})}{2\omega_0^2}\right] \mathrm{d}^2\vec{r}'$$
$$= 2\pi \int_0^D \exp\left[-\frac{(r^2 + r'^2)(1 - \mathrm{i})}{2\omega_0^2}\right] I_0\left(\frac{rr'(1 - \mathrm{i})}{\omega_0^2}\right) r' \mathrm{d}r' \tag{1}$$

where $I_0(x)$ is a zeroth order modified Bessel function of the first kind and $\omega_0 = \sqrt{L/k}$ is the waist of the minimally spreading Gaussian for that cavity (L being the cavity length, k the wavenumber $2\pi/\lambda$, with $\lambda = $1064 nm). We take the radius of the disc over which we integrate to be $D = 3.55\omega_0$. This value gives a diffraction loss in the Advanced LIGO arm cavity of approximately 0.5 ppm, as does the choice of spherical mirror parameters in the Gaussian mode case above. Knowing the field we may readily calculate the mirror profile z_{HR},

$$z_{\text{HR}}(r) = \frac{\text{Arg}[\Psi_{\text{mesa}}(r)] - \text{Arg}[\Psi_{\text{mesa}}(0)]}{k} \tag{2}$$

Construction of the mirror figure in the nearly concentric mesa case is expedited by the duality relations discovered by Agresti [13]. Using these relations one finds that the nearly concentric mesa cavity mirror profile is nothing other than a perfectly concentric sphere ($R = L/2$) with z_{HR} subtracted. More general cavities are discussed by Bondarescu and Thorne [11].

Figure 1 contrasts the intensity profiles and mirror figures of Gaussian and mesa beams for an unperturbed Advanced LIGO cavity. The figure shows clearly the point

made in the introduction that the mesa beam samples more of the mirror surface ($\sim 50\%$) than does the Gaussian beam of similar diffractive loss.
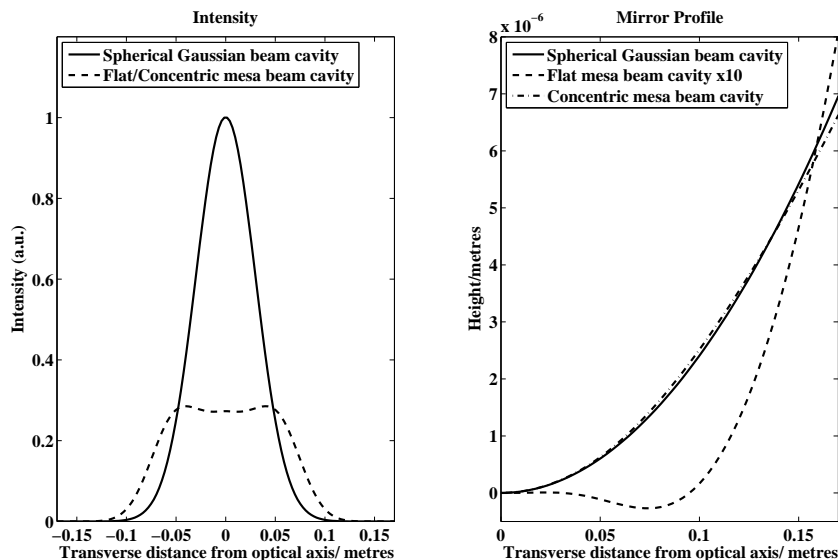
Figure 1. A comparison of mesa (dashed lines) and Gaussian (solid lines) beams and the mirrors which support them. Left: Intensity profiles normalised to have equal power. The spot size of the Gaussian beam (where the intensity falls by $1/e^2$) is 6 cm, while that of the mesa beam is $\simeq$ 12 cm; i.e. at FWHM the Gaussian beam samples $\sim$4% of the mirror's surface whereas the mesa beam samples over 27%. Right: Nominal mirror figures for an AdvLIGO cavity. The flat mesa beam mirror profile has been expanded by a factor of ten to better show its structure. The concentric mesa mirror profile is realised by subtracting the flat mesa profile from a concentric sphere with $R = L_{\text{cavity}}/2$. The abscissa extends to 0.17 m., the baseline mirror radius for AdvLIGO.

2. Simulation tools

Static Interferometer Simulation, SIS, is a program developed at Caltech/LIGO in order to study, in detail, the optical aspects of the Advanced LIGO interferometer [14]. In SIS, optical fields at mirror surfaces are evaluated over a spatial grid. The fields are propagated from mirror to mirror by first transforming them into a wave vector basis using a fast Fourier transform and then propagating the transformed field from the first mirror to the second using a paraxial approximation. At the second mirror the optical field is transformed back into a spatial basis and the transverse phase profile of the mirror applied to the field. Optical fields combining from opposite sides of a mirror surface are also summed at this point. The resolution of the simulation is determined by the shortest spatial wavelength and can be chosen as short as one needs so long as the paraxial approximation holds. In the calculations done here, the grid was 256x256 pixels on a 0.7 m square.

SIS uses an iterative procedure to find the stationary fields for a given optical configuration and input field spectrum. The mirrors' positions can be 'locked' to the appropriate fraction of an optical fringe by applying error signals calculated using standard heterodyne techniques. SIS can also calculate the signal sideband induced by small motions of the mirrors. Surface deformations, such as thermal deformation (using the Hello-Vinet approximation [15]), measured aberrations, randomly generated figure error and micro-roughness can also be included.
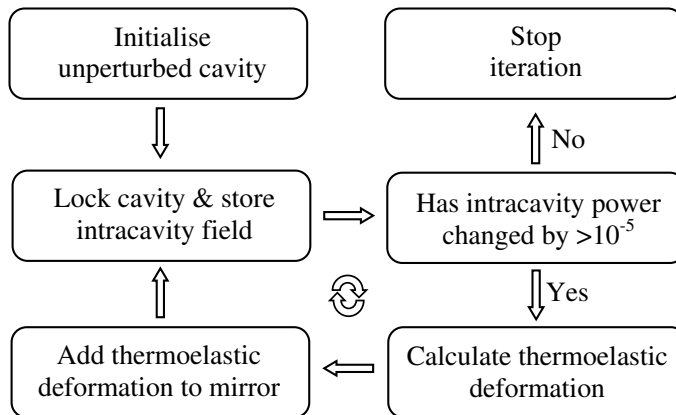
The choice of where to convert from Gaussian to mesa beams is not obvious. In this article we assume that the arm cavity is driven by a Gaussian input field. With 1070 W of power, this input gives 850 kW of circulating power in the unperturbed spherical mirror cavity, a value considered for Advanced LIGO. However, the spot size of the incident Gaussian beam differs among the three configurations: for the spherical mirror cavity it is 6 cm to match the mode resonating in the unperturbed cavity. For the mesa beam cavities the input spot size is 8.4 cm in the flat case and 8.2 cm for the concentric system, to optimise the coupling to the unperturbed cavity's mesa beam mode. This optimised coupling is 95% in both cases. Thus the power build-up in the unperturbed mesa cavities is only 808 kW‡.

In this study we sought static, self-consistent solutions of the optical fields and thermal deformations, using the following procedure: starting with an unperturbed cavity and no stored optical power, a field is injected through the input mirror, and the fields throughout the cavity propagated and updated. These fields are re-propagated and updated iteratively until the stored intracavity power is stable to one part in 10^5 between successive iterations. We then calculated the thermoelastic distortion of the mirror surfaces for this intracavity mode shape and power and some assumed mirror coating absorption§. This distortion was then added to the mirror phase profile and the optical simulation restarted with no stored intracavity power. Again we seek a stable optical solution, but generally with a different mode shape and stored power due to the distortion. The thermoelastic distortion due to this new intracavity optical field was applied to the mirrors, and the procedure repeated until the stored intracavity power is stable between the larger distortion iterations to within one part in 10^5. This process is summarised in figure 2.

We found that for low powers convergence was achieved within 10 iterations; at higher powers convergence was slower. As the system approached equilibrium the system was found to oscillate numerically between distinct optical modes and thermal distortions. These problems tended to occur at larger absorbed powers and were easily

‡ Thermorefractive aberrations will also be present in the input mirror substrate, but these have been ignored in this study so as to better understand the cavity effects. This is equivalent to assuming that the purely thermorefractive aberrations have been compensated on the input field prior to injection into the cavity. It should be noted that such compensation is far from trivial.
§ Absorption in the input mirror substrate is also generally present and also contributes to the thermoelastic deformation, but this contribution is negligible because the heating of the coating is much greater due to the high arm cavity finesse and the thermoelastic deformation of the mirror surface per unit absorbed power is much less for the substrate than coating [16].

```
┌─────────────────┐                    ┌─────────────────┐
│   Initialise    │                    │      Stop       │
│ unperturbed cavity │                  │    iteration    │
└─────────────────┘                    └─────────────────┘
         ⇓                                      ⇑ No
┌─────────────────┐      ⇒     ┌─────────────────────┐
│ Lock cavity & store │          │ Has intracavity power │
│  intracavity field  │          │  changed by >10⁻⁵   │
└─────────────────┘            └─────────────────────┘
         ⇑              ↻                   ⇓ Yes
┌─────────────────┐      ⇐     ┌─────────────────────┐
│ Add thermoelastic │          │ Calculate thermoelastic │
│ deformation to mirror │      │    deformation      │
└─────────────────┘            └─────────────────────┘
```

Figure 2. Flowchart detailing the iteration procedure used to find static self-consistent intracavity fields and the thermoelastic deformations they produce.

overcome by implementing a simple bisection procedure, averaging the perturbation of successive iterations (see figure 3).

These convergence issues are numerical rather than physical. They arise from our instantaneous approach to a system that exhibits thermal lag. Our model treats the thermal response of the mirror as being comparably rapid to the optical buildup within the cavity. In reality the cavity response is many orders of magnitude faster, and the optical field adapts nearly instantaneously to the thermal deformation of the mirror, but not vice-versa.

Nevertheless we believe that our result represents the true physical solution. If we reduce our 'step size' adding only a small portion of the mirror perturbation (reality being the limit of infinitesimal step size) we arrive at the same equilibrium, but with much slower convergence.

3. Implications for interferometric detectors

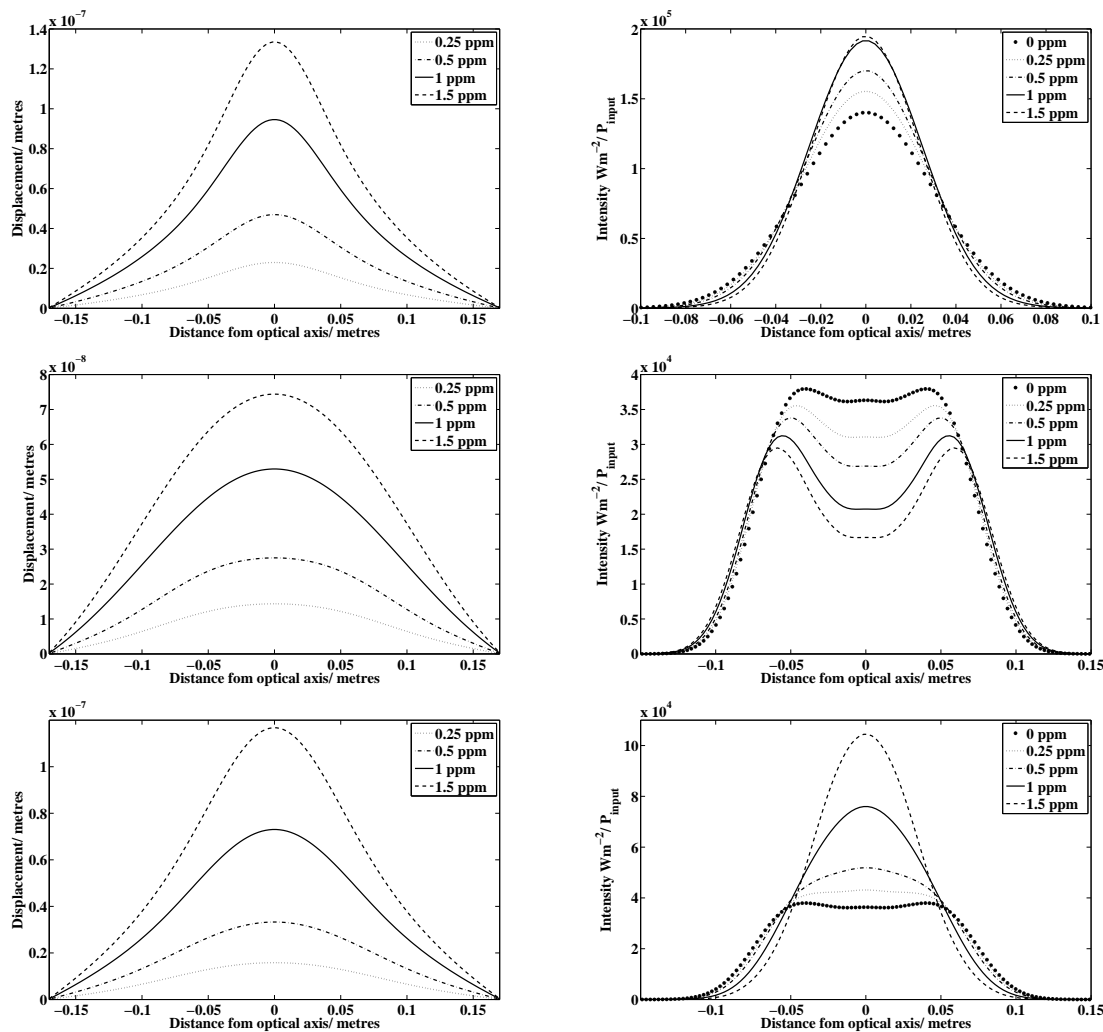### 3.1. Thermoelastic deformation and resultant mode shape

The leftmost column of figure 4 shows the deformation of the mirror profile for both mesa and Gaussian cavities. The shape of the deformation is dependent on the thermal gradients imposed by the beam. At low power levels flat and concentric mesa beams induce similar thermoelastic deformations; as greater power is absorbed the concentric beam tends toward a Gaussian intensity profile and hence gives rise to larger deformations typical of Gaussian beams. Flat mesa beams retain their greater width under thermal perturbations and produce about 50% less thermal deformation than that produced by the Gaussian mode. This is consistent with the general results of Vinet [15], and is due to the more even deposition of heat into the mirror. The mesa deformation more closely resembles a pure radius of curvature change, which can be easily compensated by heating the rear face of the mirror, an approach clearly better
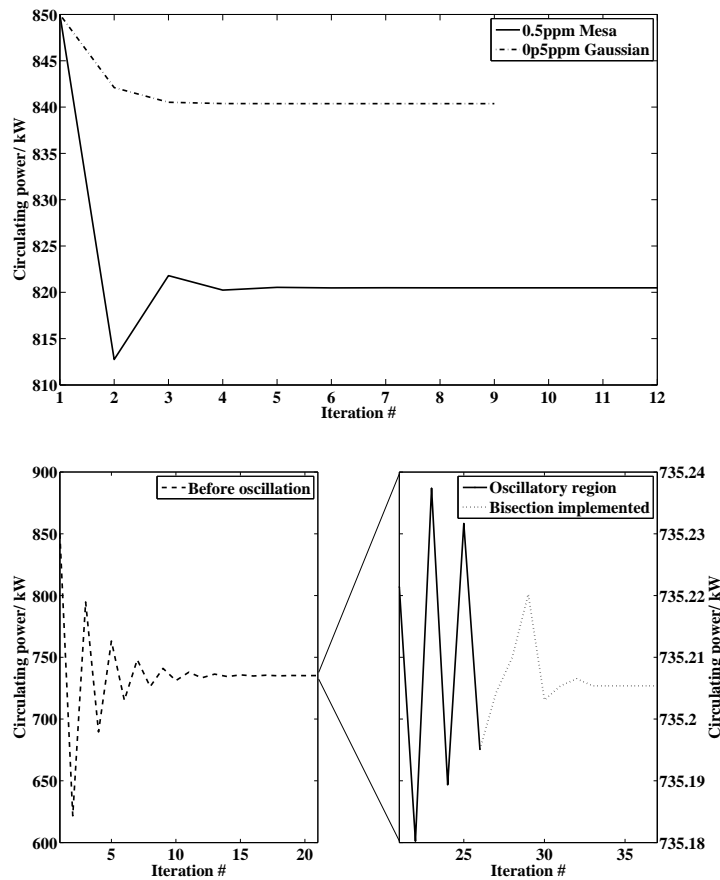
Figure 3. Top: Intracavity power as a function of iteration number for 0.5 ppm absorption. Convergence is achieved within 10 iterations in the Gaussian case; the mesa system requires 15 refinements. At higher absorption rates low level numerical oscillations were found. A simple bisection algorithm was implemented and rapid convergence achieved. The bottom panes demonstrate this in the flat mesa beam case for 2.5 ppm absorption. Bottom left: Gross convergence is achieved within 20 iterations. Bottom right: On closer inspection a low level numerical oscillation is present. Convergence is expedited by our bisection algorithm. To allow for easy comparison of different systems, the mesa intracavity powers have been normalised such that unperturbed mesa and Gaussian cavities store the same power. In reality the power stored in the mesa cavity is somewhat lower.

suited to the end test masses of gravitational wave detectors.

Although the shapes of the thermal distortions are of interest the change in the structure of the resonant light field is more important to the performance of the interferometer. The right-hand column of figure 4 shows the effects of the deformations on the cavity eigenmode. The Gaussian beam is fairly robust in its functional form as the absorbed power increases. For small amounts of heating, the spot size on the mirrors decreases, as the thermoelastic bump effectively increases the mirrors' radii of curvature, making the cavity more stable. The stored power, as we show in the next section, does not substantially decrease until the absorbed power becomes relatively large.

Figure 4. Thermoelastic deformation (left) and resonant mode shape (right) as a function of coating absorption. Top row: spherical cavity; middle row: flat mesa cavity; bottom row: concentric mesa cavity.

The mesa beam cavities, on the other hand, undergo striking changes. The flat mesa beams deform into a more annular shape, even for the smallest amounts of heating, whilst the width of the profile changes very little. This is likely to be due to confinement of the optical field by the steep rim of the mirror profile, which is not much changed by the thermal distortion. The concentric mesa beams are also grossly deformed but instead of retaining their width these beams become strongly peaked.

This differing behaviour may be understood by considering the profiles of the two mesa mirrors (see figure 1). Both mirrors are only a small deviation away from optics which support narrow Gaussian modes. The flat mesa mirror is realised by *adding* a small deviation, z_{HR}, to a flat surface; the concentric mirror constructed by *subtracting* the same small deviation from a spherical surface. Thermal effects *add* a small perturbation to the existing mirror profile making the flat mirror less flat and the concentric mirror more spherical. Hence these effects will tend to push the concentric

mesa mirror toward supporting narrower beams whilst the flat mesa mirror should be more resilient.

3.2. Losses

Given the high finesse of the arm cavities, losses are significant even at the part per million level. In table 1 we present a summary of the diffraction and mode matching losses as a function of absorbed power.

Table 1. Cavity gain and diffraction losses as a function of coating absorption. The quoted diffraction loss is for a complete round trip, losses per bounce are half as large. Mode matching losses refer to the fraction of the input beam not coupled into the cavity and are derived from the discrepancy between the theoretical and observed intracavity powers, accounting for diffraction losses but not other sources of intracavity loss (e.g. absorption).

Cavity	Coating Absorption ppm	Cavity Gain	Diffraction Loss ppm	Mode Matching Loss %
Gaussian	0	795	0.43	0
	0.25	792	0.19	< 1
	0.5	786	1.16	1
	1	755	32.42	4
	1.5	689	189.32	7
Flat Mesa	0	755	0.48	5
	0.25	747	0.80	6
	0.5	737	1.37	7
	1	717	3.20	10
	1.5	697	6.63	12
Concentric Mesa	0	756	0.49	5
	0.25	763	0.33	4
	0.5	768	0.29	3
	1	764	0.76	4
	1.5	733	6.12	8

This increased mode matching loss effectively reduces the cavity gain. The mode matching loss is also significant for any heterodyne readout scheme employing phase modulated sidebands of Gaussian profile.

The altered cavity eigenmode will not couple as strongly to the input beam. We derive this dominant mode coupling loss from a comparison between the theoretical intracavity power and that which is seen in SIS. Once diffraction effects are taken into account we attribute the residual losses to mode coupling error, in doing so we ignore other effects such as scatter and absorption. The numbers obtained using this method are in excellent agreement with those calculated directly from the inner product of the intracavity and injected fields. One could envisage mitigating these losses via thermal compensation in the recycling cavity. Such ideas are not discussed in this article.

Our calculated round trip diffraction losses for the unperturbed cavities are in accord with previously published values [7, 17]. To our knowledge the results for perturbed cavities are the first to be published.

3.3. Thermal noise

Non-Gaussian beams, including mesa beams, are being studied both theoretically and experimentally as they are expected reduce test mass thermal noise in interferometric gravitational wave detectors [10, 11, 18, 19]. Thermoelastic distortion of the cavity mirrors changes the intensity profile of the cavity mode profile and thus alters the effects of thermal noise.‖

It has been shown that a thermally perturbed spherical cavity continues to support a nearly Gaussian beam [20]. The only consequence of moderate heating is that the beam waist shrinks, increasing total thermal noise by around 10%.

Thermal effects in non-Gaussian cavities are less well understood. Using the techniques outlined in Appendix B we calculated the thermal noise expected for the perturbed eigenmodes of section 3.1. Our findings are presented in figure 5 along with the corresponding results for a Gaussian cavity.

As expected the thermal noise associated with the Gaussian and concentric mesa beams increased with absorbed power as the beam waist became smaller. The effects of beam size on thermal noise have been well documented [21, 22, 23, 24, 25]. However, the noise of the thermally perturbed flat mesa beam decreased under the same conditions. Note that these results are a strong function of the material parameters used in their evaluation, see Appendix C.

4. Thermal Compensation System

Although the above improvements in the thermal noise seen by a flat mesa beam are interesting, the modes which produce them would simultaneously reduce the sensitivity of any detector as they have a poor overlap with the Gaussian modes outside the interferometer's arms. We must maintain the standard mesa mode even if the thermal noise will be greater¶.

The Mexican hat mirrors which support mesa beams are constructed using a multi-step silica deposition process over a micro-polished flat substrate [26]. Currently this technique can achieve up to 2 nm precision and is able to create almost any mirror profile desirable in a full scale interferometric detector. Exploiting this technology we resolved to design a mirror which only achieves the correct figure after thermoelastic deformation caused by the impinging optical power. This approach would reduce the

---

‖ Strictly speaking, thermoelastic distortion is associated with increased thermal noise by virtue of the extra heat in the mirror. We ignore this effect in this article.
¶ It is of course possible to devise a scheme whereby gravitational wave readout is effected by injecting a suitable mode at the output port of the interferometer.
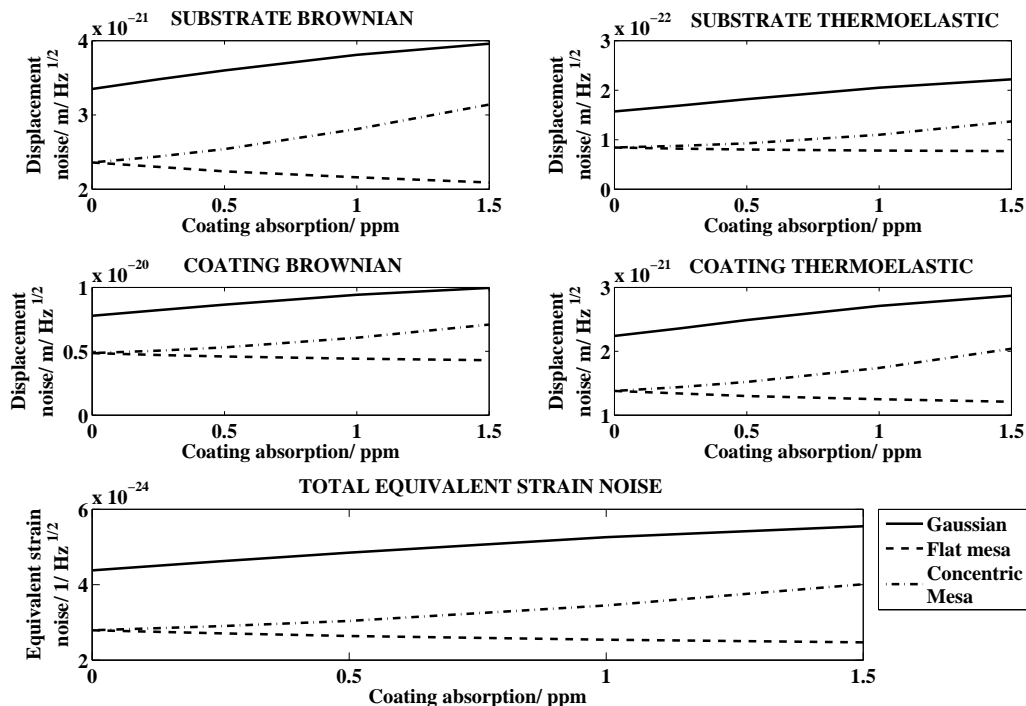
Figure 5. Thermal noise as a function of coating absorption. All values are evaluated at 100 Hz for a cylindrical fused silica substrate (34x20 cm) with a silica-tantala quarter wave coating. A full list of physical parameters is given in Appendix C. We find that the impact of thermal noise associated with mesa beams decreases as a function of coating absorption for flat configurations and increases in the concentric scheme. Total equivalent strain noise is evaluated as $\sqrt{4\sum_i N_i^2}/L$. Each N_i represents the displacement noise arising from one of the four mechanisms plotted above and L is the length of the arm cavity. This calculation assumes that all four cavity mirrors have the same coating and hence overestimates the total thermal noise.

compensation required from (and hence noise introduced by) external sources such as a carbon dioxide laser or ring heater.

4.1. Method

Using the tools developed above we are able to find the thermoelastic deformation caused by an (almost) arbitrary intensity profile. Using SIS we can find the eigenmode of a thermally perturbed cavity. The self-correcting mirror profile, giving the desired cavity eigenmode only when thermally deformed, may then be found iteratively. Beginning from an unperturbed cavity, the system is allowed to evolve to its steady state as described by figure 2. We then subtract the resulting thermoelastic deformation from the nominal mirror profiles and allow the system to reach a new steady state. Iteratively repeating this process one eventually arrives at the mirror figure which deforms under thermal loading to support the desired mode.

4.2. Results

In figure 6 below we show how such a system might operate for Gaussian and mesa modes. We chose to study the case of 0.5 ppm coating absorption, at the time of writing a typical value for future gravitational wave detectors.

4.2.1. Gaussian The upper-left plot of figure 6 shows the uncorrected deformation arising from 0.5 ppm absorption (dashed line). The solid line is the profile which must be subtracted from our cavity mirrors to restore the nominal mode. Note that these profiles are not equal. Qualitative understanding of this effect may be gained by noting that the power stored in the cavity formed by the compensating mirrors when thermal absorption is absent (upper right plot, dash-dot curve) is less than that present in the deformed cavity (upper right plot, dashed). Since less power is incident on the optics, the thermoelastic deformation induced is smaller and hence a smaller correction is necessary to restore the nominal cavity eigenmode.[+]

In the upper-right plot we outline our compensation scheme: the circular markers give the theoretical cavity eigenmode ignoring thermal effects, the dashed line represents the intensity profile to be expected if no correction is implemented. Using a dash-dot line we show the mode which is resonant when our compensating mirrors are cold. The solid line shows the intensity profile recovered once these mirrors are at operating temperature, as expected this profile agrees excellently with the ideal cavity mode.

4.2.2. Mesa The middle and bottom rows of figure 6 show analogous results for flat mesa and concentric mesa cavities respectively. For both configurations the mode recovered after heating again shows superb agreement with the nominal mode.

In order for the corrective mirror profiles calculated above to be practicable in a real interferometer we may require some auxiliary source to heat the test mass before resonance is attained (such as a carbon dioxide laser or ring heater). Once stably locked this compensating source may have its heating significantly reduced so that noise is injected at a level which is acceptable for recording astrophysical data.

The results of both of these figures neglect multiple real-world effects. For example vague knowledge or variability in the coating absorption, laser intensity noise and fabrication errors. Effects such as these were responsible for the variable success of a similar scheme used in the polishing of the initial LIGO power recycling mirrors. Nonetheless we believe that this approach merits further study.

5. Summary and discussion

We have calculated the change in the resonant mode of a mesa beam Fabry-Perot cavity as a function of coating absorption. Along with other candidates, this non-Gaussian

[+] An identical argument holds for the concentric mesa beam case whilst an analogous approach is suitable for flat mesa beams where the cold cavity stores more power and requires a correction larger than the uncorrected deformation.
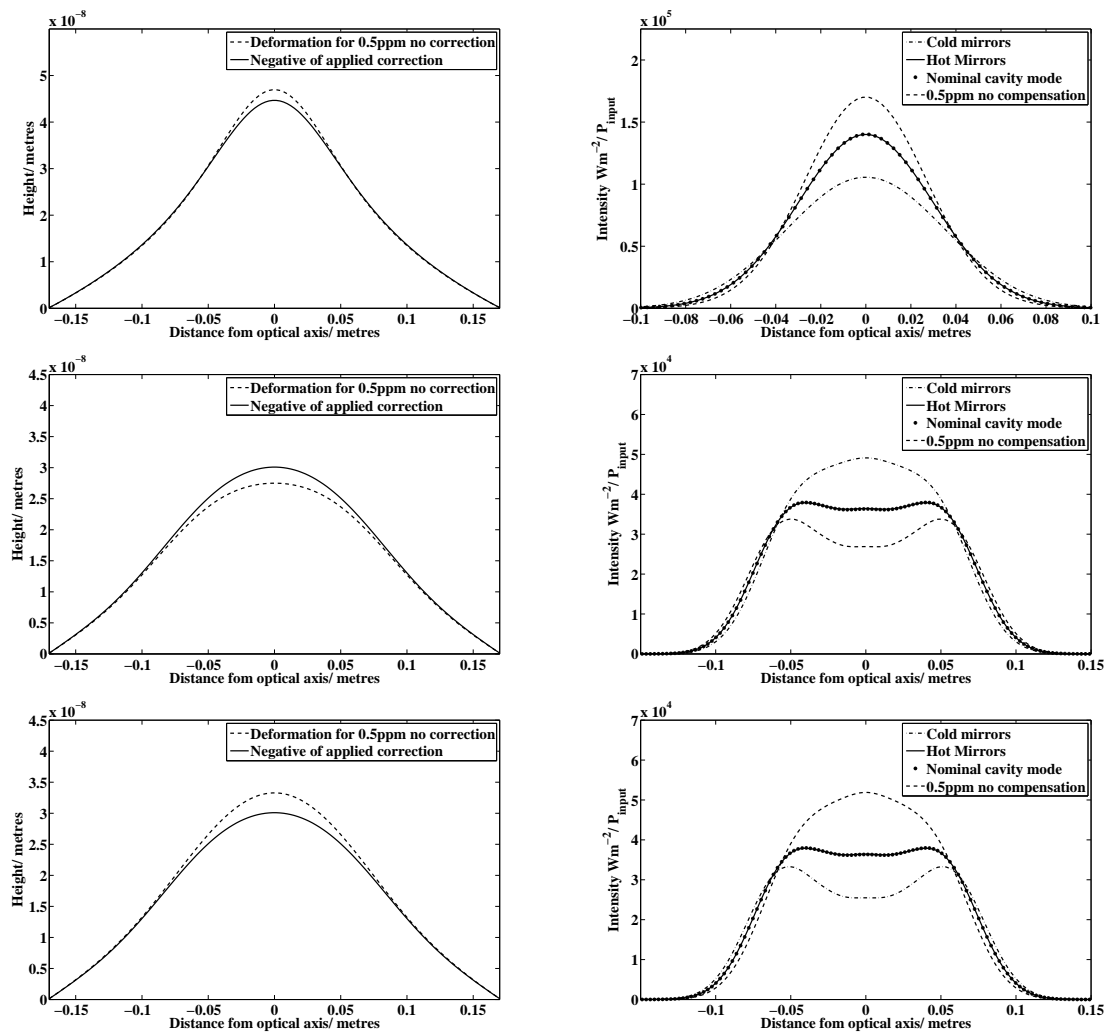
Figure 6. Thermal compensation idea: Gaussian (top row), flat mesa (middle row), concentric mesa (bottom row). Left: Thermoelastic deformation with no correction and the correction which must be subtracted to regain the nominal mode. Right: Mode profiles with no TCS (dashed), with our doctored TCS mirrors 'cold' (dash-dot) and 'hot' (solid). Note that the recovered mode (solid line) overlaps exactly with the ideal cavity mode (filled circles).

beam is being considered as an option for future interferometric gravitational wave detectors as it ameliorates the effects of test mass thermal noise. We find for flat mesa beams, in contrast to Gaussian and concentric mesa modes, that the thermal noise mitigation increases with absorbed power.

In addition we have outlined a possible passive method of thermal compensation for non-Gaussian beams. The same techniques may also be useful as an addition to TCS systems for Gaussian beams.

Acknowledgments

Appendix A. Thermoelastic deformation

We follow a well-known derivation by Hello and Vinet [15] and recent expansion by Vinet [27] which allows one to calculate the thermoelastic deformation induced in any axially symmetric mirror heated by absorption of an axially symmetric transmitted beam.

This derivation solves for the displacement of the mirror coating along the beam axis $u_z(r)$ in terms of a Dini expansion:

$$u_z(r) = \sum_m U_m(1 - J_0(\zeta_m r/a)) - \frac{1-\nu}{2Y}Br^2 \tag{A.1}$$

where ζ_m is the mth root of $\zeta J_1(\zeta) - \tau J_0(\zeta) = 0$, $\tau = 4\sigma' T^3 a/K_{\text{th}}$ being the reduced radiation constant and a the radius of the mirror. The coefficients U_m are given by

$$U_m = \frac{\alpha(1+\nu)\epsilon P_{\text{L}}a^2}{K_{\text{th}}} \sum_m \frac{p_m}{\zeta_m} \frac{\zeta_m + \chi - (\zeta_m - \chi)\exp(-2\zeta_m h/a)}{(\zeta_m + \chi)^2 - (\zeta_m - \chi)^2\exp(-2\zeta_m h/a)} \tag{A.2}$$

where $\quad p_m = \frac{1}{P_{\text{L}}} \frac{2\zeta_m^2}{a^2(\chi^2 + \zeta_m^2)J_0^2(\zeta_m)} \int_0^a |\Psi(r)|^2 J_0(\zeta_m r/a)r\mathrm{d}r \tag{A.3}$

P_{L} is the power circulating in the cavity and ϵ is a coating absorption rate so that the product $P_{\text{L}}\epsilon$ gives the total absorbed power in the coating, h is the thickness of the mirror, and α and ν are the mirror thermal expansion coefficient and Poisson's ratio. The second term of $u_z(r)$ is the Saint-Venant term, in which Y is the mirror Young's modulus. The calculation of B is given by Hello and Vinet [15].* This term acts to make the thermal deformation more convex.

Figure A1 shows how efficiently the Dini expansion reconstructs both Gaussian and mesa profiles. Excellent fidelity is achieved with few terms. Our analysis is adaptive, unconditionally implementing the first ten terms with subsequent terms being added if they are within a factor of 10^{-6} of the principal term. For the unperturbed beams this corresponds to over 80 terms.

---

* The sign of the Saint-Venant correction is incorrect in Hello and Vinet's final result, and has been corrected here.
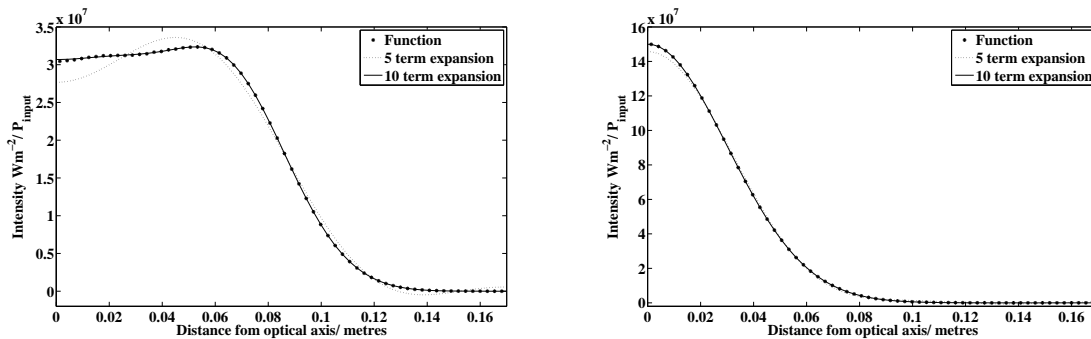
Figure A1. Much of the work described herein relies on Dini expansions. Here we show how efficiently the Dini expansion is able to approximate our two beams under study. Left: A recreation of the mesa beam (asterisks) using 5 and 10 terms. Right: An analogous plot for Gaussian beams. The functions are well reconstructed with a minimum of terms.

Appendix B. Thermal noise

In [28] Levin takes a fluctuation-dissipation theorem approach to thermal noise calculation, we follow his example. The spectral density of displacement noise due to thermal effects is given by

$$S_X(\omega) = \frac{8k_{\mathrm{B}}T}{\omega^2}\frac{W_{\mathrm{diss}}}{F_0^2} \tag{B.1}$$

where W_{diss} is the average energy dissipated in the region of interest (coating or substrate) in response to an applied oscillatory pressure

$$P(\vec{r},t) = \Re(F_0 f(\vec{r})\exp(\mathrm{i}\omega t))$$

which has the same spatial distribution, $f(\vec{r})$, as the intensity of the beam under study. Our task is to calculate W_{diss} for each of the dissipative mechanisms in which we are interested.

In this section, to maintain agreement with previous publications, the test mass occupies the region $r \in [0,a]$, $z \in [-h/2, 0]$, with the coated surface at $z = 0$.

Appendix B.1. Stresses and strains

In order to calculate W_{diss} - and therefore the thermal noise associated with our perturbed modes - we must first find the stresses and strains in the substrate and coating. Here we adopt the techniques of BHV [29] subsequently corrected by Liu & Thorne [30].

Again we form a solution in terms of Dini expansions, seeking displacements of form:

$$u_r(r,z) = \sum_m A_m(z)J_1(k_m r) \tag{B.2}$$

$$u_z(r,z) = \sum_m B_m(z)J_0(k_m r) \tag{B.3}$$

$$u_\phi(r, z) = 0 \tag{B.4}$$

The calculation of the A_m and B_m follows (33-35) of Liu and Thorne [30]. To take account of the intensity profile, $|\Psi(r)|^2$, of our thermally perturbed beams (36) takes the form,

$$p_m = \frac{1}{P_L} \frac{2}{a^2 J_0^2(\zeta_m)} \int_0^a |\Psi(r)|^2 J_0(\zeta_m r/a) r \mathrm{d}r \tag{B.5}$$

With knowledge of the displacement vectors we can readily calculate the stresses and strains in the substrate via the standard relations [31].

The stresses and strains throughout the coating are a linear combination of those in the substrate, (A4) of Harry *et al.* [23] give the necessary detail. We calculate the Lamé parameters in the coating, taking account of the high and low index materials, using average values for Y and ν. These averages are calculated using the volumetric averaging operator introduced by Fejer [25]. We are now in a position to calculate the magnitudes of the thermal noise in its various forms.

Appendix B.2. Substrate Brownian Thermal Noise

Brownian noise [29] in solids is the thermally excited motion associated with its intrinsic internal damping (i.e., damping not associated with thermoelasticity). The key to reducing this internal damping is to choose a substrate material having a small loss angle $\Phi(\omega)$ or equivalently a high mechanical quality factor.

With estimates of Φ and having calculated the relevant stresses and strains above we adopt the approach expounded in section V of Liu and Thorne [30]. We only depart from their method in the calculation of the expansion coefficients p_m where we use the values given by (B.5).

Appendix B.3. Substrate Thermoelastic Thermal Noise

Thermoelastic noise is present in materials with a non-zero thermal expansion coefficient undergoing thermal fluctuations [24], and can dominate the thermal noise for certain substrate materials.

To calculate the impact of this thermoelastic noise we again turn to the arguments set forth by Liu & Thorne [30]. The frequency at which we apply the fictitious pressure to the test mass is much more rapid than the characteristic timescale for heat flow in the substrate, so we may assume a quasistatic system in which the temperature evolves adiabatically. Then the computation of W_diss reduces to evaluating

$$W_\mathrm{diss} = 2\pi K_\mathrm{ths} T \left(\frac{Y\alpha}{(1-2\sigma)C_\mathrm{v}}\right)^2 \frac{1}{2} \int_0^h \int_0^a (\nabla\Omega)^2 r \mathrm{d}r \mathrm{d}z \tag{B.6}$$

where $\Omega = \nabla \cdot \vec{u}$ is the divergence of the displacements calculated in Appendix B.1.

Appendix B.4. Coating Brownian Thermal Noise

We evaluate the Brownian noise in the coating using a model developed by Harry *et al.* [23]. This model allows for the anisotropic layered structure of the coating and assumes that the losses occur inside the materials themselves rather than at the interfaces between coating layers. As stated for Brownian noise in the substrate, the loss angle is of critical importance. In our calculations we assume equality between loss angles parallel and perpendicular to the coated surface, i.e. $\Phi_{\parallel} = \Phi_{\perp}$ in Harry's (15).

Appendix B.5. Coating Thermoelastic Thermal Noise

As with Brownian noise, thermoelastic noise is present in both the substrate and the coating. One can simplify the calculation of the coating contribution by assuming that the multi-layer coating may be well-approximated by a uniform layer having appropriately averaged properties.

Because the coating is very thin, the characteristic time scale for heat flow is short, and we can no longer take it that heat flow normal to the coating is adiabatic, hence we must adopt a perturbative approach. For a comprehensive description of the methods used please see Fejer *et al.* [25]. We embark on our analysis from a one dimensional (that dimension normal to the coated surface) thermal conductivity equation [32], our goal is to find the thermal field $\Upsilon(z,t)$:

$$\frac{\partial \Upsilon_j}{\partial t} - \kappa_j \frac{\partial^2 \Upsilon_j}{\partial z^2} = -\frac{Y_j \alpha_j T}{(1 - 2\sigma_j)C_{\mathrm{v}j}} \frac{\partial}{\partial t} \sum_{i=1}^{3} E_{0,ii,j} \tag{B.7}$$

Here the j subscript acts as a place holder for s or c meaning substrate or coating, we must solve this equation in both regions. $\kappa_j = K_{\mathrm{th}j}/C_{\mathrm{v}j}$ is the thermal diffusivity and $E_{0,ii,j}$ is the zeroth order (i.e. that due to the applied oscillatory Levin force) i-polarised compressional strain. We seek solutions enforcing the following:

$$\Upsilon_{\mathrm{c}}|_{z=d} = \Upsilon_{\mathrm{s}}|_{z=d} \tag{B.8}$$

$$K_{\mathrm{thc}}\frac{\partial \Upsilon_{\mathrm{c}}}{\partial z}\bigg|_{z=d} = K_{\mathrm{ths}}\frac{\partial \Upsilon_{\mathrm{s}}}{\partial z}\bigg|_{z=d} \tag{B.9}$$

$$\frac{\partial \Upsilon_{\mathrm{c}}}{\partial z}\bigg|_{z=0} = 0 \tag{B.10}$$

$$\frac{\partial \Upsilon_{\mathrm{s}}}{\partial z}\bigg|_{z=h} = 0 \tag{B.11}$$

i.e. continuity of temperature at the coating-substrate boundary and zero heat flux at the surfaces of the test mass. Our equations are the same as (17) in Fejer [25] except for (B.11), where we assume a mirror of finite thickness, rather than the infinite half-plane Fejer studies. The substrate is so much thicker than the coating that this leads to no quantitative difference in the result.

The equations are now simply solved and, applying the boundary conditions, we have expressions for Υ_{c} and Υ_{s}. Using the standard expression for the rate of

thermoelastic deformation

$$W_{\text{diss}} = \left\langle \int_{\text{test mass}} \frac{K_{\text{th}}}{T} (\nabla \delta T)^2 \mathrm{d}V \right\rangle \tag{B.12}$$

with $\Upsilon = \delta T$ we can compute W_{diss} as follows

$$W_{\text{diss}} = \frac{1}{2} \left(\frac{K_{\text{thc}}}{T} 2\pi \int_0^d \int_0^a |\nabla \Upsilon_{\text{c}}|^2 r \mathrm{d}r \mathrm{d}z + \frac{K_{\text{th}}}{T} 2\pi \int_d^h \int_0^a |\nabla \Upsilon_{\text{s}}|^2 r \mathrm{d}r \mathrm{d}z \right) \tag{B.13}$$

Appendix C. Material parameters

As far as possible we use the expected AdvLIGO values.

Table C1. The material parameters used in our calculations.

	Parameter	Symbol	Value
Substrate	Radius	r	0.17 m.
	Thickness	h	0.2 m.
	Density	ρ	2.2×10^3 kgm^{-3}
	Poisson ratio	σ	0.17
	Young's modulus	Y	7.2×10^{10} Nm^{-2}
	Loss angle	Φ	5×10^{-9}
	Linear thermal expansion coeff.	α_{TH}	5.1×10^{-7} K^{-1}
	Thermal conductivity	K_{th}	1.38 Wm^{-1}K^{-1}
	Specific heat at const. volume	C_{v}	1.64×10^6 JK^{-1}m^{-3}
High n	Refractive index	n_{ch}	2.03
material	Density	ρ_{ch}	6.85×10^3 kgm^{-3}
	Poisson ratio	σ_{ch}	0.23
	Young's modulus	Y_{ch}	1.4×10^{11} Nm^{-2}
	Loss angle	Φ_{ch}	3.8×10^{-4}
	Linear thermal expansion coeff.	α_{ch}	3.6×10^{-6} K^{-1}
	Thermal conductivity	K_{thch}	33 Wm^{-1}K^{-1}
	Specific heat at const. volume	C_{vch}	2.1×10^6 JK^{-1}m^{-3}
	Layer thickness ($\lambda_{LASER}/4n_{\text{ch}}$)	d_{ch}	1.31×10^{-7} m
Low n	Refractive index	n_{cl}	1.45
material	Density	ρ_{cl}	2.2×10^3 kgm^{-3}
	Poisson ratio	σ_{cl}	0.17
	Young's modulus	Y_{cl}	7.2×10^{10} Nm^{-2}
	Loss angle	Φ_{cl}	1×10^{-4}
	Linear thermal expansion coeff.	α_{cl}	5.1×10^{-7} K^{-1}
	Thermal conductivity	K_{thcl}	1.38 Wm^{-1}K^{-1}
	Specific heat at const. volume	C_{vcl}	1.64×10^6 JK^{-1}m^{-3}
	Layer thickness ($\lambda_{\text{LASER}}/4n_{\text{cl}}$)	d_{cl}	1.83×10^{-7} m

Table C2. Averaged material parameters used in the evaluation of thermal noise in the SiO_2/Ta_2O_5 coating of a test mass.

	Parameter	Symbol	Value
Average coating values	Poisson ratio	σ_{cavg}	0.195
	Young's modulus	Y_{cavg}	1.003×10^{11} Nm^{-2}
	Loss angle	Φ_{cavg}	2.167×10^{-4}
	Linear thermal expansion coeff.	α_{cavg}	1.798×10^{-6} K^{-1}
	Thermal conductivity	K_{thcavg}	2.297 Wm^{-1}K^{-1}
	Specific heat at const. volume	C_{vcavg}	1.832×10^{6} JK^{-1}m^{-3}
	Total coating thickness	d	5.975×10^{-6} m.

References

[1] Lück H *et al* 2006 *Class. Quant. Grav.* **23** S71
[2] Acernese F *et al* 2006 *Class. Quant. Grav.* **23** S635
[3] Waldman S *et al* 2006 *Class. Quant. Grav.* **23** S03
[4] Harry G M, Armandula H, Black E, Crooks D R M, Cagnoli G, Hough J, Murray P, Reid S, Rowan S, Sneddon P, Fejer M M, Route R and Penn S D 2006 *App. Opt.* **45** 1569–1574
[5] D'Ambrosio E 2003 *Phys. Rev. D* **67** 10
[6] D'Ambrosio E, O'Shaughnessy R, Strigin S, Thorne K S and Vyatchanin S 2004 *ArXiv General Relativity and Quantum Cosmology e-prints* (*Preprint* gr-qc/0409075)
[7] O'Shaughnessy R, Strigin S and Vyatchanin S 2004 *ArXiv General Relativity and Quantum Cosmology e-prints* (*Preprint* gr-qc/0409050)
[8] Savov P and Vyatchanin S 2006 *Phys. Rev. D* **74** 082002–+ (*Preprint* arXiv:gr-qc/0409084)
[9] Ballmer S, Frolov V, Lawrence R, Kells W, Moreno G, Mason K, Ottaway D, Smith M, Vorvick C, Willems P and Zucker M 2005 Thermal Compensation System Description Tech. Rep. LIGO-T050064-00-R LIGO Laboratory, California Institute of Technology
[10] Tarallo M, Miller J, Agresti J, D'Ambrosio E, Riccardo DeSalvo D F, Bernard Lagrange J M, Michel C, Montorio J, Morgado N, Pinard L, Remilleux A, Simoni B and Willems P 2007 *App. Opt.* **46** 6648–6654
[11] Bondarescu M and Thorne K S 2006 *Phys. Rev. D* **74** 082003–+
[12] Kogelnik H and Li T 1966 *App. Opt.* **5** 1550–+
[13] Agresti J, Chen Y, D'Ambrosio E and Savov P 2005 *ArXiv General Relativity and Quantum Cosmology e-prints* (*Preprint* gr-qc/0511062)
[14] Yamamoto H 2007 SIS (Stationary Interferometer Simulation) Manual Tech. Rep. LIGO-T070039-00-E LIGO Laboratory, California Institute of Technology
[15] Hello P and JY-Vinet 1990 *J. Phys. France* **51** 2243
[16] Lawrence R 2003 *Active Wavefront Correction in Laser Interferometric Gravitational Wave Detectors* Ph.D. thesis Massachusetts Institute of Technology
[17] Bhawal B 2005 Diffraction losses of various modes in advanced LIGO arm cavity Tech. Rep. LIGO-T050234-00-E LIGO Laboratory, California Institute of Technology
[18] Mours B, Tournefier E and Vinet J Y 2006 *Class. Quant. Grav.* **23** 5777–5784
[19] Bondarescu M 2007 *Topics in general relativity* Ph.D. thesis California Institute of Technology
[20] Smith M and Willems P 2007 Auxiliary optics support system conceptual design document, vol. 1 thermal compensation system Tech. Rep. LIGO-T060083-01-D LIGO Laboratory, California Institute of Technology
[21] Bondu F, Hello P and Vinet J Y 1998 *Phys. Lett. A.* **246** 227
[22] Braginsky V, Gorodetsky M and Vyatchanin S 1999 *Phys. Lett. A.* **264** 1

[23] Harry G M, Gretarsson A M, Saulson P R, Kittelberger S E, Penn S D, Startin W J, Rowan S, Fejer M M, Crooks D R M, Cagnoli G, Hough J and Nakagawa N 2002 *Class. Quant. Grav.* **19** 897–917 (*Preprint* `arXiv:gr-qc/0109073`)

[24] Braginsky V B and Vyatchanin S P 2003 *Physics Letters A* **312** 244–255 (*Preprint* `arXiv:cond-mat/0302617`)

[25] Fejer M M, Rowan S, Cagnoli G, Crooks D R, Gretarsson A, Harry G M, Hough J, Penn S D, Sneddon P H and Vyatchanin S P 2004 *Phys. Rev. D* **70** 082003–+ (*Preprint* `arXiv:gr-qc/0402034`)

[26] Simoni B 2004 *Design and Construction of a Suspended Fabry-Perot Cavity for Gaussian and Non-Gaussian Beam Testing. Preliminary Test with Gaussian Beam* Master's thesis Università di Pisa

[27] Vinet J 2007 *Class. Quant. Grav.* **24** 3897–3910

[28] Levin Y 1998 *Phys. Rev. D* **57** 659–663 (*Preprint* `arXiv:gr-qc/9707013`)

[29] Bondu F, Hello P and Vinet J Y 1998 *Physics Letters A* **246** 227–236

[30] Liu Y T and Thorne K S 2000 *Phys. Rev. D* **62** 122002–+ (*Preprint* `arXiv:gr-qc/0002055`)

[31] Landau L and Lifshitz E 1986 *Theory of Elasticity* 3rd ed (Oxford: Pergamon)

[32] Lifshitz R and Roukes M L 2000 *Phys. Rev. B* **61** 5600–5609 (*Preprint* `arXiv:cond-mat/9909271`)